

RSR-NF: Neural Field Regularization by Static Restoration Priors for Dynamic Imaging

Berk Iskender^{1,*} Sushan Nakarmi² Nitin Daphalapurkar² Marc L. Klasky² Yoram Bresler¹

¹University of Illinois at Urbana-Champaign, IL, US ²Los Alamos National Laboratory, NM, US

Abstract

Dynamic imaging involves the reconstruction of a spatio-temporal object at all times using its undersampled measurements. In particular, in dynamic computed tomography (dCT), only a single projection at one view angle is available at a time, making the inverse problem very challenging. Moreover, ground-truth dynamic data is usually either unavailable or too scarce to be used for supervised learning techniques. To tackle this problem, we propose RSR-NF, which uses a neural field (NF) to represent the dynamic object and, using the Regularization-by-Denoising (RED) framework, incorporates an additional static deep spatial prior into a variational formulation via a learned restoration operator. We use an ADMM-based algorithm with variable splitting to efficiently optimize the variational objective. We compare RSR-NF to three alternatives: NF with only temporal regularization; a recent method combining a partially-separable low-rank representation with RED using a denoiser pretrained on static data; and a deep-image prior-based model. The first comparison demonstrates the reconstruction improvements achieved by combining the NF representation with static restoration priors, whereas the other two demonstrate the improvement over state-of-the-art techniques for dCT.

1. Introduction

1.1. Dynamic Imaging

Dynamic imaging addresses the ill-posed problem of reconstructing a time-varying object from its undersampled measurements. In the extreme case, these measurements are time-sequential, meaning that only a single measurement is available at any given time instant. This problem arises in many areas of science and engineering, including dynamic computed tomography (dCT), [1–13], dynamic MRI

(dMRI) [14–20], photoacoustic CT (PACT) [21, 22], and dynamic 3D scene representation [23–29].

Dynamic imaging is more challenging compared to its static version since different measurements in the undersampled set belong to essentially different objects. Thus, the traditional algorithms for static reconstruction lead to severe artifacts, which is particularly evident for time-sequential acquisition.

In this paper, focusing on the dCT problem, we introduce a new approach and algorithm, capable of reliable reconstruction even in the extreme case of fully time-sequential acquisition where a single projection at a single view angle at a time is acquired from a highly dynamic object. The experiments in this paper address dCT, but the proposed approach is applicable to other dynamic imaging modalities. To limit the scope of the discussion though, we restrict here our review of previous work mostly to dCT and to the closely related problem of dMRI.

1.2. Related Previous Work

To address the challenging ill-posed problem in dCT and dMRI, a common general approach has been to represent or model the underlying dynamic object using a reduced number of degrees of freedom. See [11, 13] for a detailed overview of previously proposed techniques. We highlight below those that are most relevant to the work in this paper.

Low rank methods. These methods model the underlying object as low-rank in one of two ways: (i) either enforcing this as a hard constraint via a partially-separable model (PSM), which uses a low-rank factorization of the object into spatial and temporal factors [7–9, 14–16, 30–34], recently augmented by pre-learned spatial priors [10–13]; or (ii) promoting the low rank structure by including nuclear or more general Schatten- p norm penalties in the optimization objective, often with sparsity regularization in a transform domain [35–37]. Other such methods decompose the object into the sum of low-rank and sparse components, again promoting low-rankness via nuclear or Schatten- p norms [38, 39], with a recent method also decomposing the mean signal as a third component [17].

Recent low-rank methods with pre-learned spatial priors

*Corresponding author: berk.iskender@analog.com. Currently at Analog Garage, Analog Devices, Inc., Boston, MA, US.

This research was supported in part by Los Alamos National Labs under Subcontract No. 599416/CW13995.

[10–13] were shown to provide considerable improvements over other low-rank alternatives with simpler priors, and over Deep Image Prior (DIP)-based techniques [18]. However, as demonstrated by direct evaluation in Section 4.4, they may not provide sufficiently accurate reconstructions when the underlying dynamic object is high-rank.

Motion estimation and compensation. Another group of algorithms tries to recover the object using motion estimation and compensation methods [40–43]. Estimating a continuous motion field, these methods assume fixed total density and they are unable to represent topological changes (See Section 1.3 for further discussion of these limitations.)

Deep image prior. Recent dynamic imaging algorithms apply the deep learning (DL)-based deep image prior (DIP) [44] idea to spatio-temporal signals to represent the dynamic object at each time instant using a low-dimensional latent representation [18, 19]. The latent representations drive a generator neural network (NN) producing the estimated object. Here the NN parameters and potentially the latent representations [45] are estimated in an unsupervised manner. Later work combines a low-rank PSM representation with the DIP framework [20]. Drawbacks of the DIP methods include the need for early stopping to avoid overfitting and degradation which is difficult without a ground-truth oracle, difficult convergence requiring multiple random initializations, and lack of a mechanism to incorporate a prior other than indirectly and coarsely through the choice of deep NN architecture.

Neural fields. Neural fields (NFs), or implicit neural representations, have been proposed lately as DL-based continuous representations of natural scenes and static and dynamic objects in a wide range of applications [46]. In particular, applications in computed imaging include static CT [47–50] and MRI [49], dCT [51–53] and dMRI [54–57], dynamic PACT [21, 22], cryo-EM [58], and medical imaging in general [59]. A NF representation is particularly effective in dynamic imaging problems since it is essentially resolution-free, and the number of parameters to represent, and also the memory required to store the object do not scale with the spatio-temporal resolution.

For dCT, several methods [51–53, 60] decouple the reconstruction into recovering a reference (“template”) cross-section or volume via a spatial NF, and estimating a motion field to represent the dynamics by warping the template. These methods are subject to limitations similar to those of other motion field-based techniques (see above). For dynamic PACT, some NF-based methods [21, 22] use a partition of unity NN (POUnet) [61] as the NF architecture to represent the dynamic object, which is claimed to improve performance over that by a standard NF. In our experiments in Section 4.4, we compared the representation power of a POUnet with that of a standard NF with positional encoding, and did not encounter a notable difference.

In the computed dynamic imaging applications discussed above, similar to PSM or DIP-based methods, most of the NF-based models are fitted in an unsupervised manner, using only the measurement data to estimate the NN parameters. Also, regularization in addition to the NF, if any, is in the form of traditional, fixed regularizers. This misses the opportunity to use more powerful learning-based targeted regularization.

Sharing some elements with the proposed approach, a recent method for *static* sparse-view CT [62] combines a NF representation for the object with a learned regularizer using the RED framework [62]. Due to high computational load, the regularization is performed on a subset of blocks of the estimated object for each update of the NF parameters. However, even with this strategy, sweeping blockwise over the entire object remains computationally heavy. The reconstruction quality is similar to that of the comparison benchmarks. Furthermore, despite using in RED an artifact removal NN as in RARE [63] instead of a denoiser, the NN is trained in a supervised manner. Unfortunately, such an approach is not feasible for the majority of dynamic imaging problems, including dMRI and dCT where there is no ground-truth dynamic data.

1.3. Proposed Approach

To overcome the limitations of previous methods, while still utilizing learned spatial priors as in [10–13], we propose the reconstruction algorithm *Regularization by Static Restoration* priors with a *Neural Field* (RSR-NF) for dynamic imaging, which uses a neural field to provide a highly expressive yet parsimonious representation for the spatio-temporal object, and combines it with a smoothness prior for temporal regularization, and with a pre-learned spatial restoration prior using the RED framework [64], to enable recovery in critically undersampled scenarios. The latter feature allows RSR-NF to exploit the performance of a restoration network pre-trained on available *static* ground-truth data. To solve the resulting non-convex optimization problem, we use an ADMM algorithm with an efficient fixed-point update for the spatial regularizer.

RSR-NF offers several advantages over previous NF-based reconstruction methods for dynamic imaging. Importantly, unlike [52], RSR-NF does not require ground-truth dynamic data. Furthermore, in contrast to the NF-based algorithms such as [51–53, 60] that recover a static template and the corresponding motion field to warp it, RSR-NF does not make the assumption of a fixed total density, which may be restrictive (e.g, injecting a contrast agent to the field-of-view, or cross-slice motion while imaging a fixed slice can violate this assumption). Another issue with the motion field-based methods is their inability to represent topological changes, which require discontinuity in the representation [27]. Finally, compared to the NF-based approach

in [21], which uses simpler regularizers, the variational objective in RSR-NF is regularized with more accurate, pre-learned spatial priors.

Contributions. (1) To the best of our knowledge, RSR-NF is the first method for dynamic object reconstruction, to combine NF-based object representation with a pre-learned, static spatial prior. (2) RSR-NF does not require *spatio-temporal* training data, which is typically unavailable or very difficult to obtain. RSR-NF is therefore applicable to a wide range of dynamic inverse problems. (3) Unlike methods such as [65], which use a deep NN regularizer, the optimization scheme in RSR-NF avoids costly backpropagation computations through the deep restoration NN for updating the NF parameters.

2. The dCT Imaging Inverse Problem

In dCT the objective is to reconstruct a spatio-temporal object $f(\mathbf{x}, t)$, $\mathbf{x} \in \mathbb{R}^d$ (with $d = 2$ or $d = 3$ for individual slice or volumetric reconstruction), from its projections

$$g(\cdot, \theta, t) = \mathcal{R}_\theta\{f(\mathbf{x}, t)\} + \eta(\cdot, \theta, t) \quad (1)$$

obtained using the Radon transform operator \mathcal{R}_θ at view angle θ and corrupted by additive noise η . Considering the extreme case of time-sequential sampling with only one projection acquired at each time instant with uniform temporal spacing, the set of measurements is

$$\{g(s, \theta_p, t_p)\}_{p=0}^{P-1}, \quad \forall s, t_p = p\Delta t, \quad (2)$$

where s is the offset of the line of integration from the origin (i.e., detector position), and P is the total number of projections (and temporal samples) acquired. Sufficient sampling of the variable s is assumed, and it is suppressed in the following notation. The angular sampling scheme, $\{\theta_p\}_{p=0}^{P-1}$, with $\theta_p \in [0, 2\pi]$, is a free design parameter.

This ill-posed inverse problem is particularly challenging since, in the time-sequential setting, each projection belongs to a different object. This is a significant drop from the required more than C projections for the artifact-free reconstruction of a static object of a diameter of C -pixels. To address this issue, several techniques [2, 3, 6] cluster temporally adjacent projections and model the object as static during their acquisition. However, this reduces the temporal resolution, and any departure from this assumption (as in the case of time-sequential sampling) gives rise to modeling inaccuracies in the measurement fidelity term, leading to reconstruction errors.

On the other hand, in certain cases, pre- and post-motion static reconstructions of the dynamic object, or reconstructions of similar static objects are available and can be exploited to improve the estimated solution accuracy. This is the scenario we address.

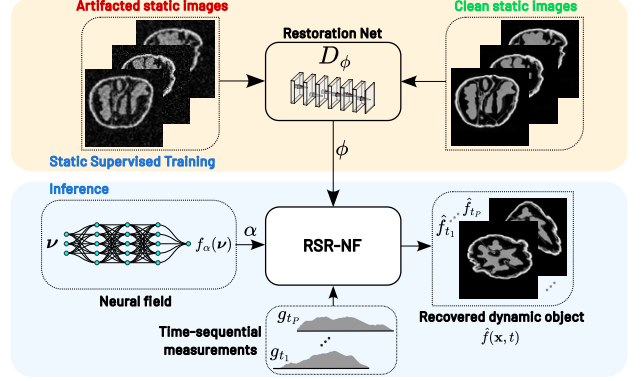


Figure 1. The RSR-NF framework. The deep restoration network D_ϕ is trained on slices of *static* objects similar to the object of interest, and the learned spatial prior is used at inference time.

3. Proposed Method: RSR-NF (Figure 1)

3.1. Neural field representation for the object f

To represent the complete 2D dynamic object f , we use a standard neural field $N_\alpha : \mathbb{R}^3 \rightarrow \mathbb{R}$ where the temporal coordinate is also added to the input as $\nu = (\mathbf{x}, t)$ with all coordinates normalized such that $\nu \in [0, 1]^3$, and α represents the learnable parameters. The NF has a MLP architecture using fixed Fourier positional encodings $\gamma(\nu) \in \mathbb{R}^{L \times 6}$ with L linearly increasing frequencies [47] to mitigate spectral bias [66], where the l -th row is defined as $\gamma(\nu)_l = (\sin(\pi l/2\nu), \cos(\pi l/2\nu))$ where $l \in \{1, \dots, L\}$, and \sin and \cos are applied to coordinate vectors element-wise. The positional encodings are followed by a MLP network $M_\alpha : \mathbb{R}^{L \times 6} \rightarrow \mathbb{R}$ mapping the encoded coordinates to the estimated output densities. Thus, the overall NF model computes the density values $\mu_\nu \in \mathbb{R}$ at a given spatio-temporal coordinate $\nu \in \mathbb{R}^3$ as

$$f^\alpha(\nu) = M_\alpha(\gamma(\nu)) = \mu_\nu.$$

3.2. Variational Formulation and Optimization

The variational objective to be optimized is

$$\begin{aligned} \min_{\alpha, \tilde{f}} \sum_t \|g_{\theta(t), t} - R_{\theta(t)} \tilde{f}_t^\alpha\|_2^2 + \lambda \rho(\tilde{f}_t) + \xi \rho_\tau(\tilde{f}^\alpha) \\ \text{s.t. } \tilde{f}^\alpha = \tilde{f} \end{aligned} \quad (3)$$

where $g_{\theta(t), t} \in \mathbb{R}^J$ is the measured time-sequential projection at time t and view angle $\theta(t)$ corrupted with AWGN, $\tilde{f}^\alpha \in \mathbb{R}^{J^2 \times P}$ is the neural field representation of the object f^α rendered on a fixed, spatially-vectorized $J^2 \times P$ grid aligned with the space-time coordinates, and $\tilde{f}_t^\alpha \in \mathbb{R}^{J^2}$, $t = 0, \dots, P-1$ is its t -th time instant (“frame”), and $R_{\theta(t)} : \mathbb{R}^{J^2} \rightarrow \mathbb{R}^J$ is the discretized Radon transform operator at view angle $\theta(t)$. The temporal regularizer ρ_τ is a finite difference approximation to the energy in the second

order derivative with respect to time $\|\partial^2 f / \partial t^2\|_F^2$,

$$\rho_\tau(\tilde{f}^\alpha) = \sum_{t=2}^{P-1} \|\tilde{f}_{t-1}^\alpha - 2\tilde{f}_t^\alpha + \tilde{f}_{t+1}^\alpha\|_2^2.$$

The spatial regularizer ρ with weight $\lambda > 0$ is the RED term

$$\rho(\bar{f}_t) = \bar{f}_t^T (\bar{f}_t - D_\phi(\bar{f}_t)) \quad (4)$$

where $D_\phi : \mathbb{R}^{J^2} \rightarrow \mathbb{R}^{J^2}$ is a restoration operator that takes a single time frame f_t of the object as input and produces its restored version as output. RED [64] was originally inspired by the PnP method [67, 68], which uses a denoiser to replace a proximal mapping and proposed the explicit regularizer (4) with a denoiser D . RED has been widely used for static reconstruction tasks [69–71], and was recently applied to dynamic imaging [11, 13]. The original theoretical analysis [64] has assumptions that are not simultaneously satisfied for many denoisers but the score-matching framework in [72] explains good performance in such cases.

Similar to recent works [62, 63, 73, 74], we replace the denoiser with a learned deep NN restoration operator D_ϕ . (See Section 3.3 for further details of D_ϕ .) Note that in (3) and (4), the spatial regularizer ρ is applied to auxiliary variable \bar{f} , rather than directly to the NF output \tilde{f}^α . However, using the NF representation for the RED updates in solving the optimization problem (3) would require costly back-propagation computations through the deep restoration NN for updating the NF parameters. To avoid this, we perform the variable splitting $\tilde{f}^\alpha = \bar{f}$, and in (3) and (4), the spatial regularizer ρ is applied to auxiliary variable \bar{f} , rather than directly to the NF output \tilde{f}^α . The split variable $\bar{f} \in \mathbb{R}^{J^2 \times P}$ is constrained to equal the rendered NF representation \tilde{f}^α .

To solve the resulting problem, we use an ADMM framework similar to [10, 11]. This time the variable split is performed on the NF representation instead of the low-rank bilinear PSM. The resulting augmented Lagrangian in the scaled form [75, 76] is

$$\begin{aligned} \mathcal{L}_\beta[\tilde{f}^\alpha, \bar{f}; \gamma] = & \sum_t \left(\left\| R_{\theta_t} \tilde{f}^\alpha e_t - g_t \right\|_2^2 + \lambda \rho(\bar{f} e_t) \right) \\ & + \xi \rho_\tau(\tilde{f}^\alpha) - \frac{\beta}{2} \|\gamma\|_F^2 + \frac{\beta}{2} \|\tilde{f}^\alpha - \bar{f} + \gamma\|_F^2, \end{aligned} \quad (5)$$

where $\gamma \in \mathbb{R}^{J^2 \times P}$ is the dual variable and $\beta > 0$ is the augmented Lagrangian weight.

The proposed RSR-NF algorithm minimizes (5) with respect to the primal variables \tilde{f}^α and \bar{f} and performs a dual ascent step for γ . The method is described in Algorithm 1. Step 2 of the algorithm is solved iteratively using gradient descent for a fixed number of updates per each outer iteration. The number of outer iterations I is selected sufficiently high for convergence or marginal improvements with additional iterations.

Step 3 can be replaced by a fixed-point update with early stopping [10–12]. Using the gradient rule

$$\nabla \rho(\bar{f}_t) = \bar{f}_t - D_\phi(\bar{f}_t),$$

this leads to the efficient single use of the restoration NN D_ϕ at each outer iteration in Algorithm 2.

3.3. Learning static restoration priors

Various strategies have been proposed to utilize restoration priors in different settings. As an unsupervised alternative, RARE [63] trains an image prior using reconstructions obtained from undersampled measurements and replaces the deep denoiser in the RED [64] framework by an artifact removal NN. However, RARE may struggle for severely undersampled problems such as dCT with time-sequential measurements without assumptions such as clustering temporally adjacent projections. Instead, RSR-NF uses supervised pre-training on relevant ground-truth static data.

The replacement of the denoiser in a RED or PnP framework by a restoration operator is motivated by recent work [73, 74] that has shown that pre-trained restoration models can function as effective priors for unseen inverse problems, performing on par or better than the traditional or even diffusion model-based denoisers in RED and PnP.

Similar to the regularization denoisers in [10, 11, 70], the restoration deep NN in RSR-NF D_ϕ has a DnCNN architecture [77]. If available, the NN is pre-trained on a training set of 2D slices of similarly distributed *static* objects. In the absence of such data, if the object is dynamic for a period of time and static otherwise, the training is performed using pre and post-motion static slices of the same object. This strategy is agnostic to the specific dynamic behavior of the object of interest. The variational objective for the super-

Algorithm 1 RSR-NF

input: $\alpha^{(0)}, \bar{f}^{(0)} = \tilde{f}^\alpha{}^{(0)}, \gamma^{(0)}, \beta > 0, \lambda > 0, \xi > 0$

- 1: **for** $i \in \{1, \dots, I\}$ **do**
 - 2: $\alpha^{(i)} = \arg \min_{\alpha} \{ \sum_t \|g(\cdot, \theta(t), t) - R_{\theta(t)} \tilde{f}_t^\alpha\|_2^2 + \frac{\beta}{2} \|\tilde{f}_t^\alpha + \gamma_t^{(i-1)} - \bar{f}_t^{(i-1)}\|_F^2 + \xi \rho_\tau(\tilde{f}^\alpha) \}$
 - 3: $\forall t : \bar{f}_t^{(i)} = \arg \min_{\bar{f}_t} \{ \lambda \rho(\bar{f}_t) + \frac{\beta}{2} \|(\tilde{f}_t^{\alpha^{(i)}} + \gamma_t^{(i-1)}) e_t - \bar{f}_t\|_2^2 \}$
 - 4: $\gamma^{(i)} = \gamma^{(i-1)} + \bar{f}^{\alpha^{(i)}} - \bar{f}^{(i)}$
 - 5: **end for**
-

Algorithm 2 RSR-NF with efficient f -step

Notes: Inputs, and Lines 1-2 and 4-5 are the same as Algorithm 1. The \bar{f} -step is applied $\forall t$.

- 3: $\forall t : \bar{f}_t^{(i)} = \frac{\lambda}{\lambda + \beta} D_\phi(\bar{f}_t^{(i-1)}) + \frac{\beta}{\lambda + \beta} (\tilde{f}_t^{\alpha^{(i)}} + \gamma_t^{(i-1)})$
-

vised pretraining of the NN is

$$\min_{\phi} \sum_i \|f_i - D_{\phi}(\hat{f}_i)\|_F^2 \text{ s.t. } \hat{f}_i = H_i f_i + \eta_i, \forall i, \quad (6)$$

where to allow the NN is to correct various levels of artifacts and hence to diversify the ensemble of restoration scenarios, similar to [74, 78], we set H_i to a convex combination of the identity map I and the degradation operator G_i as $H_i = \zeta_i G_i + (1 - \zeta_i)I$ where $\zeta_i \sim U[0, 1]$. We select G_i as Gaussian blur operator with kernel size k_i , and to further diversify the ensemble of restoration scenarios, we randomize the kernel size $k_i \sim U[0, k_{\max}]$. The injected noise $n_i \sim \mathcal{N}(0, \sigma_i^2 I)$ has noise level $\sigma_i \sim U[0, \sigma_{\max}]$.

4. Experiments

4.1. Datasets

Compressed polymer. The dataset of a porous polymer under compression was generated at the Los Alamos National Laboratory by physics-based numerical simulation as the temporal evolution of the coordinates of finite element nodal positions. The material is a polymer with a cellular structure under quasi-static compression where the complete temporal evolution consists of 1001 time frames. The high computational load and the inability to compare the accuracy against real-world data prevents the use of multiple such simulations for supervised learning. For a voxel-based representation, we first create a 4D $128 \times 128 \times 128 \times 1001$ spatio-temporal grid with the object at $t = 0$ at the center, and map each node in all time frames to the corresponding voxel. The mapping is binary, such that the voxel density is 1 if there are one or more nodes that are mapped to it, and 0 otherwise. Then, we conduct our experiments on the $128 \times 128 \times 1001$ fixed 48th axial slice of the 3D dynamic object in Figure 2. Due to memory constraints, we partition the 1001 frames into 7 non-overlapping intervals of length $128 + \text{one of } 105 \text{ frames}$, and conduct experiments on the interval shown in Figure 2. This intermediate difficulty interval (#2) was chosen after ranking the intervals based on the accuracies of their NF embeddings using a fixed architecture and the same number of iterations.

Walnut dataset. We utilize reconstructions of two distinct (static) walnuts from the publicly accessible 3D walnut CT dataset [79]. To generate a dynamic test object, we synthetically warp the central axial slice of one walnut using a sinusoidal piecewise-affine time-varying warp [80]. This 2D image is divided into an $N \times N$ uniformly spaced rectangular grid, and the vertical displacement of $\Delta_{n,t} = -C(t) \sin(3\pi n/N)$, $n \in \{0, \dots, N - 1\}$ is applied on each row independently to create the temporal warp, where $C(t)$ is a linearly increasing function of t with $C(0) = 0$. The static axial, coronal, and sagittal slices of the other walnut are employed to train the restoration NN.

For both datasets, time-sequential projection data is simulated from the dynamic object, and used as the measurement data in experiments as described in Section 4.3.

4.2. Comparison Benchmarks

FBP: To demonstrate the difficulty of the dynamic reconstruction problem, we directly reconstruct the object from its P undersampled time-sequential projections using traditional filtered backprojection (FBP) with a Ram-Lak filter. Since FBP can only reconstruct a static instance, we use sliding windows of size $P/2$ with overlap $P/2-1$ for each time frame.

TD-DIP [18]: TD-DIP is an unsupervised DIP-based algorithm, proposed for dMRI. For dCT, we replace the forward operator with the 2D Radon transform $R_{\theta(t)}$. TD-DIP uses fixed latent representations to incorporate a motion-specific prior and subsequent two-stage deep neural network architecture to generate the estimated object at each time instant.

RED-PSM [10, 13]: RED-PSM combines an object-domain low-rank PSM with RED [64], and the resulting optimization objective is minimized using a bilinear ADMM algorithm with convergence guarantees. To accelerate and improve convergence, the method can use a fast projection-domain PSM [7, 8] estimate for initialization.

Temp-NF: As a key ablation study, we compare RSR-NF to Temp-NF – a version eliminating the spatial prior by setting $\lambda = 0$ in (3) but keeping the temporal regularization.

4.3. Experimental Settings

All experiments were conducted on a workstation with an Intel(R) Xeon(R) Gold 5320 CPU and NVIDIA RTX A6000 GPU. The optimization subproblem for the NF parameters in Algorithm 2 was solved using SGD with the Adam [81] optimizer. For each update, mini-batches of $P/8$ projections were sampled at random (with replacement) from the entire set of P projections.

Restoration Network and Pre-training. As in [10–12], each convolutional layer in the restoration CNN D_{ϕ} is followed by a ReLU nonlinearity, except for the final single output channel layer. One restoration NN was pre-trained for each of the two objects. The upper limits for the noise level and blur kernel size for training D_{ϕ} were set to $\sigma_{\max} = 5 \cdot 10^{-2}$ and $k_{\max} = 2$ pixels, respectively. For the dynamic walnut object, D_{ϕ} is trained on the central 200 axial, 200 sagittal, and 200 coronal slices of another static walnut CT reconstruction downsampled to size 128×128 . For the compressed polymer, a total of 422 axial, sagittal, and coronal slices of the pre- and post-compression objects were used for pre-training. Importantly, although we experiment on a temporal subinterval of the full dynamic object, we do not assume the availability of the beginning and end frames of the subinterval for training.

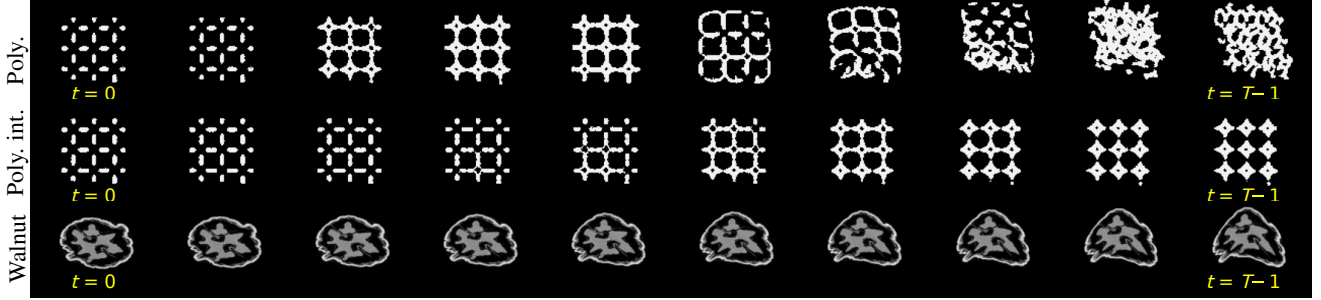


Figure 2. Ground-truth frames of different dynamic objects. Compressed polymer uniformly sampled in time : full spatio-temporal object for $T=1001$ (top); the second non-overlapping subinterval with $T=128$ (center). Warped walnut for $T = 128$ (bottom).

Tomographic Acquisition Scheme. The acquisition of projection data in the parallel beam geometry is simulated by applying a numerical forward projection operator to the dynamic object data at different time instants, to produce P projections. To simulate a realistic noise level, the projections are corrupted by additive white Gaussian noise of intensity chosen such that a conventional Ram-Lak FBP reconstruction of the static version of the object from $P = 512$ such projections will have a PSNR of 46 dB.

All methods here employ the bit-reversed angular sampling scheme over the range $[0, \pi]$ for the projection angles $\{\theta_p\}_{p=0}^{P-1}$, as described in Section 2. Compared to alternative time-sequential acquisition schemes, this scheme has been shown [7, 8] to provide better conditioning of the forward operator. Although the bit-reversed scheme requires increased rotation speed, in certain applications such as MRI with radial acquisition, CT scanner with electronic beam deflection [82], or in scenarios where the acquisition time of a single projection dominates the rotation time (e.g., because of low source photon flux or a dense material), this does not constitute a problem. In addition, in physically constrained settings, the number of distinct views can be reduced and these views can be repeated periodically, facilitating implementation by multiple source-detector pairs, or by carbon nanotube sources [83, 84]. This scenario is studied in one of the experiments reported in Section 4.4.

NF architecture and initialization. Unless stated otherwise, the NF used in the experiments consists of $L = 10$ Fourier positional encodings for each of the input coordinates with linearly increasing frequencies in the interval $[\pi/2, L\pi/2]$ [47] followed by a MLP architecture with 7 hidden layers of width 64 and ReLU nonlinearities with randomly initialized parameters α . The number of hidden layers were chosen as $h = 7$ such that it provides sufficient expressivity for our experiments. Indeed, for L sinusoidal encodings the maximum encoding frequency is $L\pi/2$, and for resolution $J = 128$ of the sampling grid the expressivity analysis in [85] predicts at least $\log_2(\frac{J\pi}{L\pi/2}) < 5$ hidden layers to achieve the maximum frequency on the grid without aliasing. Hence, this is satisfied with some margin by the choice of $h = 7$.

Evaluation Metrics. To evaluate the performance of the compared methods, we use the peak signal-to-noise ratio (PSNR) in dB, the structural similarity index (SSIM) [86], the mean absolute error (MAE), and the high-frequency error norm [87] as $\text{HFEN}(f, f_r) \triangleq \|\text{LoG}(f) - \text{LoG}(f_r)\|_2$ where LoG is the rotationally symmetric Laplacian of Gaussian filter with a standard deviation of 1.5 pixels.

4.4. Results

Embedding experiments. We compare the representation accuracies of the proposed NF model with the partition of unity NF (POUnet) NN architecture [21] and with low-rank PSM for different numbers of degrees of freedom (parameters in the NF model). We perform this comparison on full data (not projection measurements) of the compressed polymer data subinterval. For the PSM, we show the rank- K approximation accuracies obtained by truncating the SVD of the object f to the first K dominant components. For the two NF representations, we evaluate embeddings with different numbers of MLP layers and channels per layer. The NF parameters are optimized by the Adam optimizer with 125K iterations and learning rate of $5 \cdot 10^{-3}$.

Qualitative comparison of representations at different time instants using the low-rank PSM and the proposed NF architecture is shown in Figure 3 for the polymer subinterval. In the comparison, the NF uses 7 layers and 64 channels per layer, and the PSM has a rank of 3 which leads to a similar number of free parameters for both alternatives. As can be seen in the absolute error figures, the NF provides substantial accuracy improvements for both objects, whereas the PSM leads to over-smoothed representations.

We also provide PSNR (in dB) comparisons for various representations with different number of degrees of freedom in Figure 3. The results verify that for similar numbers of free parameters, NF-based representations with various widths and depths provide significant improvements over the PSM. The NF architecture used in this work and the POUnet alternative of [21] provide similar representation accuracies for a similar number of free parameters. However, for polymer subinterval, when the number of degree of freedom is small, the proposed architecture provides im-

provement over the POUnet.

Another aspect in the comparison of the PSM vs. NF approaches, is that for each K , the accuracy for the object SVD truncated to rank K constitutes an upper bound on the ℓ_2 sense performance of the rank- k PSM. Conversely, for the NF embeddings, changes in the optimization scheme may enable further accuracy improvements.

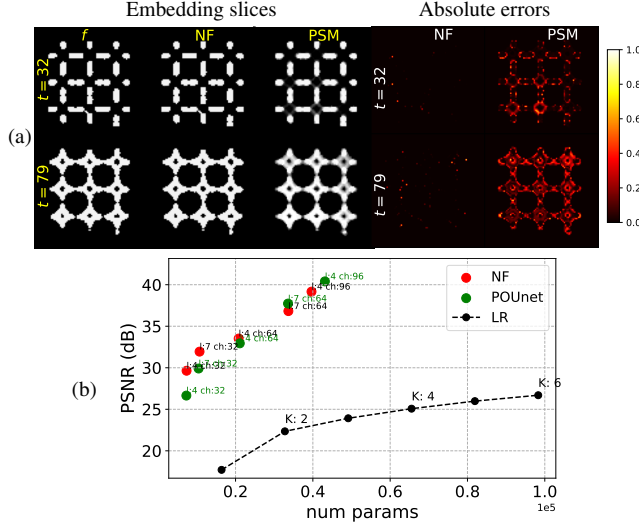


Figure 3. (a) Representations & corresponding absolute errors for $T=128$ polymer time frames at two times for NF embedding with 7 layers and 64 channels per layer and for a rank- $K=3$ PSM, which has roughly $1.5\times$ more parameters than the NF. (b) Representation PSNR (in dB) for different NF architectures and rank- K PSM.

dCT reconstruction accuracies for different P . We compare RSR-NF with four different benchmarks: (i) FBP; (ii) TD-DIP [18]; (iii) RED-PSM [10–12]; and (iv) Temp-NF. This comparison is done on the warped walnut and on the polymer subinterval, using the time-sequential projection data. See Supplementary Material Table 2 for the parameter configurations for the various methods. The accuracy metrics of the various reconstructions vs. number of time-sequential measurements P are shown in Figure 6. For each P , the accuracies are calculated only based on the P frames from which the projections are obtained. A more precise comparison of the plotted accuracies are provided in Table 1.

For both objects and for various P , the RSR-NF reconstructions with learned static spatial priors have substantially improved metrics over RED-PSM and TD-DIP, and also improve consistently over the ablated version with only temporal regularization, Temp-NF.

To visually assess the temporal resolution of the different methods, Figure 7 compares reconstructed $x-t$ "slices" through the walnut and the compressed polymer, taken at the locations indicated by a yellow line on the static $x-y$ frame at $t = 0$. As highlighted for the walnut by an arrow and for the polymer by the green box on the respective

ground-truth $x-t$ slices, RSR-NF has higher temporal resolution and outperforms the comparison benchmarks.

In Figure 8, we provide a qualitative comparison of reconstructions for $P = 128$ at three different time instants for the dynamic walnut. To facilitate comparison, we include only the three best-performing methods in the figure, RSR-NF, Temp-NF and RED-PSM. Compared to RED-PSM, RSR-NF suppresses the errors further. Specifically, as shown in the zoomed-in region indicated by the yellow box, the high-frequency features around the shell of the walnut are recovered with greater accuracy by RSR-NF, whereas the RED-PSM suffers from over-smoothing. On the other hand, focusing on the zoomed-in region indicated by green boxes, RSR-NF provides better recovery of the uniform density regions of the walnut.

Likewise, Figure 9 compares reconstructions of the polymer subinterval for $P = 128$ at three different time instants. Again, we include the same three methods, RSR-NF, Temp-NF and RED-PSM. As expected from the results in Figure 6, RSR-NF improves over the other methods, particularly visible at $t = 49$. To facilitate the comparison, we provide, in addition to the RSR-NF reconstructions, the absolute reconstruction error maps.

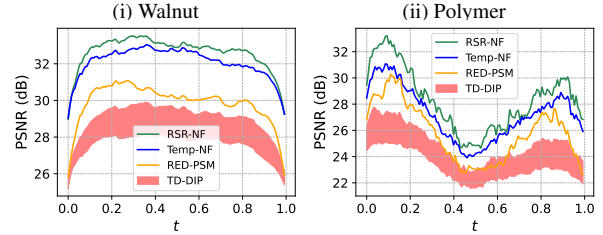


Figure 4. Reconstruction PSNR vs. t for (i) walnut and (ii) polymer. The shaded area for TD-DIP shows the interval between the best and the worst PSNR in three runs with random initialization.

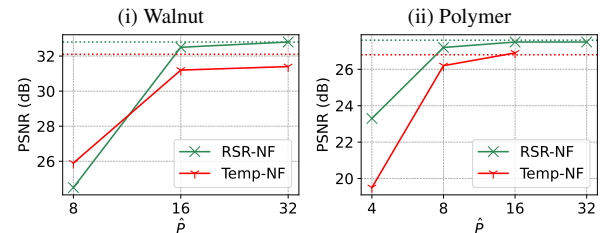


Figure 5. Reconstruction PSNR vs. number of distinct view angles \hat{P} with $P = 128$ for (i) walnut, and (ii) polymer subinterval.

Smaller number of distinct view experiments. Since accessing a complete set of distinct view angles sequentially while using view angle schemes such as bit-reversed can be physically challenging, we also tested RSR-NF and its ablated version without spatial priors, Temp-NF, in a setting with only $\hat{P} < P$ distinct view angles that are sampled using the bit-reversed pattern, with the pattern repeated to produce a total of $P = 128$ projections. All other parameters

	P	Method	PSNR (dB)	SSIM	MAE (1e-3)	HFEN
Walnut	32	FBP	15.1	0.300	8.4	2.13
		TD-DIP (L)	22.5	0.882	2.1	0.87
		RED-PSM	22.8	0.911	1.5	0.78
		Temp-NF	23.7	0.937	1.4	0.71
		RSR-NF	24.4	0.946	1.3	0.65
	64	FBP	18.3	0.387	5.4	2.04
		TD-DIP (L)	25.6	0.916	1.5	0.74
		RED-PSM	26.4	0.958	0.9	0.57
		Temp-NF	28.0	0.974	0.8	0.49
		RSR-NF	29.4	0.982	0.7	0.40
	128	FBP	20.3	0.503	3.8	2.22
		TD-DIP (L)	29.0	0.953	1.0	0.50
		RED-PSM	30.3	0.979	0.6	0.40
		Temp-NF	32.1	0.988	0.5	0.33
		RSR-NF	32.8	0.988	0.5	0.32
Polymer	32	FBP	9.6	0.292	22.69	50.1
		TD-DIP (L)	21.1	0.850	3.09	9.67
		RED-PSM	20.2	0.865	2.42	10.92
		Temp-NF	21.6	0.954	1.88	9.15
		RSR-NF	22.3	0.967	1.41	7.83
	64	FBP	14.4	0.352	12.30	35.6
		TD-DIP (L)	23.5	0.915	2.13	8.59
		RED-PSM	22.7	0.917	1.51	9.74
		Temp-NF	24.1	0.977	1.20	8.22
		RSR-NF	24.8	0.983	0.84	7.33
	128	FBP	17.1	0.466	7.64	31.49
		TD-DIP (L)	24.3	0.849	2.41	10.58
		RED-PSM	25.3	0.940	0.98	9.68
		Temp-NF	26.8	0.986	0.74	8.31
		RSR-NF	27.6	0.988	0.55	7.35

Table 1. Reconstruction accuracies for different P for dynamic walnut, and compressed polymer subinterval. For TD-DIP, the reported accuracies are for the best PSNR using a “stopping oracle”, averaged over three runs with random initial conditions.

were kept constant during the comparisons.

The reconstruction PSNRs vs. \hat{P} for the two objects are shown in Figure 5. The dashed lines indicate the performance of *each method* in the ideal case of $\hat{P} = P = 128$. While RSR-NF is robust to the decrease in number of distinct view angles, Temp-NF degrades more compared to $\hat{P} = P$ for the walnut for $\hat{P} > 8$. At $\hat{P} = 8$ the PSNR degrades considerably for both methods. For the polymer, both methods show a similar trend compared to the $\hat{P} = P$ case, but Temp-NF exhibits a sharper decline for $\hat{P} = 4$.

These results show the potential of RSR-NF under physical constraints where the number of distinct view angles is reduced by eight or sixteen fold, with no performance loss.

5. Conclusions

We proposed RSR-NF, which is, to the best of our knowledge, the first NF-based dynamic imaging method with pre-learned spatial priors. The proposed ADMM algorithm for optimization of the variational objective is computationally efficient, by avoiding costly backpropagation through the deep regularizer NN for NF updates. Embedding experiments show significantly better embedding accuracy for a similar number of degrees of freedom by the NF than by a low-rank representation. Reconstruction experiments show

improved accuracies for RSR-NF compared to three benchmarks: a recent PSM-based alternative, RED-PSM; a DIP-based method; and a NF-based method without the learned spatial priors and with only temporal regularization. The dCT study highlights however the necessity for temporal regularization when the problem is severely undersampled.

Future work may include exploration of different initialization types, comparison with recent NF-based methods proposed for different inverse problems by adapting them to dCT, and application of RSR-NF to different imaging scenarios.

References

- [1] P. Willis and Y. Bresler, “Optimal scan for time-varying tomography. I. Theoretical analysis and fundamental limitations,” *IEEE Transactions on Image Processing*, vol. 4, no. 5, pp. 642–653, 1995. 1
- [2] K. A. Mohan *et al.*, “TIMBIR: A method for time-space reconstruction from interlaced views,” *IEEE Transactions on Computational Imaging*, vol. 1, no. 2, pp. 96–111, 2015. 3
- [3] G. Zang *et al.*, “Space-time tomography for continuously deforming objects,” *ACM Trans. Graph.*, vol. 37, no. 4, pp. 100:1–100:14, Jul. 2018. 3
- [4] X. Huang *et al.*, “U-net-based deformation vector field estimation for motion-compensated 4D-CBCT reconstruction,” *Medical Physics*, vol. 47, no. 7, pp. 3000–3012, 2020.
- [5] F. Madesta *et al.*, “Self-contained deep learning-based boosting of 4D cone-beam CT reconstruction,” *Medical Physics*, vol. 47, no. 11, pp. 5619–5631, 2020.
- [6] S. Majee *et al.*, “Multi-slice fusion for sparse-view and limited-angle 4D CT reconstruction,” *IEEE Transactions on Computational Imaging*, vol. 7, pp. 448–462, 2021. 3
- [7] B. Iskender *et al.*, “Dynamic tomography reconstruction by projection-domain separable modeling,” in *2022 IEEE 14th Image, Video, and Multidimensional Signal Processing Workshop (IVMSP)*. IEEE, 2022. 1, 5, 6
- [8] B. Iskender *et al.*, “Dynamic tomography reconstruction by projection-domain separable modeling,” *arXiv:2204.09935*, 2022. 5, 6
- [9] B. Iskender *et al.*, “Factorized projection-domain spatio-temporal regularization for dynamic tomography,” in *2023 IEEE International Conference on Acoustics, Speech and Signal Processing*. IEEE, 2023. 1
- [10] B. Iskender, M. L. Klasky, and Y. Bresler, “RED-PSM: Regularization by denoising of partially separable models for dynamic imaging,” in *Proceedings of the IEEE/CVF International Conference on Computer Vision (ICCV)*, October 2023, pp. 10 595–10 604. 1, 2, 4, 5, 7
- [11] B. Iskender, M. L. Klasky, and Y. Bresler, “RED-PSM: Regularization by denoising of partially separable models for dynamic imaging,” in *2023 IEEE/CVF International Conference on Computer Vision (ICCV)*, 2023, pp. 10 561–10 570. 1, 4
- [12] B. Iskender, M. L. Klasky, and Y. Bresler, “Dynamic tomography reconstruction via low-rank modeling with a RED spatial prior,” in *2023 IEEE 9th International Workshop on Computational Advances in Multi-Sensor Adaptive Processing (CAMSAP)*. IEEE, 2023, pp. 506–510. 4, 5, 7
- [13] B. Iskender, M. L. Klasky, and Y. Bresler, “RED-PSM: Regularization by denoising of factorized low rank models for dynamic imaging,” *IEEE Transactions on Computational Imaging*, pp. 1–16, 2024. 1, 2, 4, 5
- [14] Z.-P. Liang, “Spatiotemporal imaging with partially separable functions,” in *2007 4th IEEE international symposium on biomedical imaging: from nano to macro*. IEEE, 2007, pp. 988–991. 1

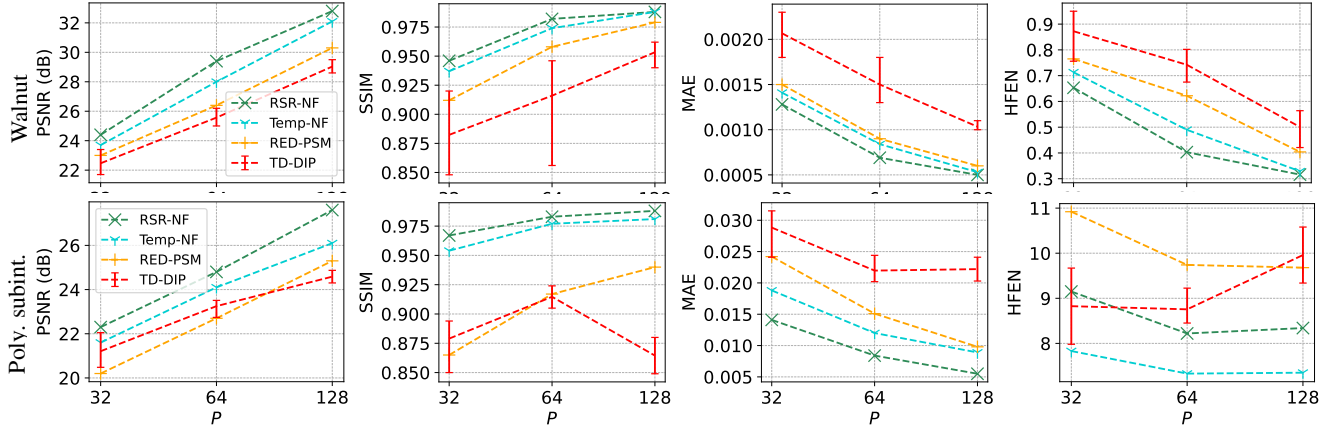


Figure 6. Reconstruction metrics for the time-varying walnut and compressed polymer vs. P using different methods. For TD-DIP, the metrics reported are assuming a “stopping oracle” that stops the iterations at the best PSNR reconstruction.

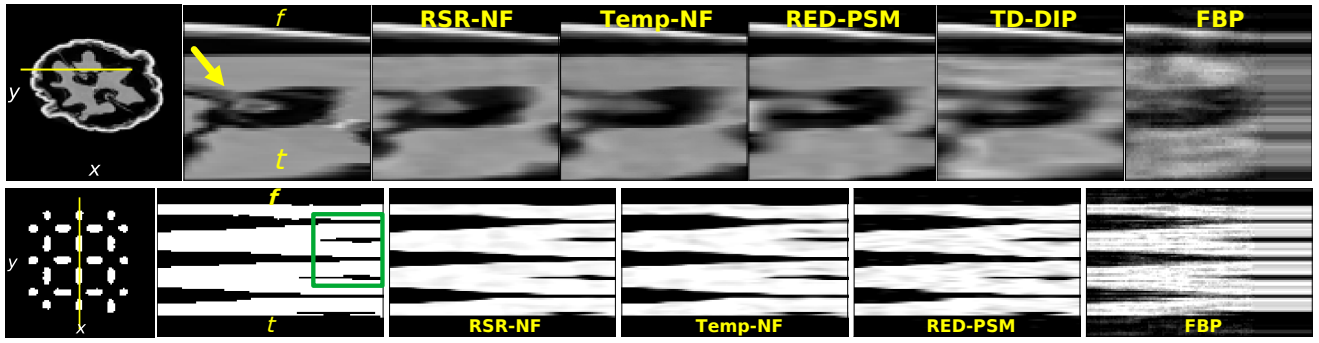


Figure 7. Comparison of reconstructed x - t slices using different methods for dynamic walnut (top) and compressed polymer (bottom) for $P = 128$. The cross-sections are shown on the static $t = 0$ objects with a yellow line. The x - y coordinates are indicated in white on the static objects and t coordinate is shown on the slices of f in yellow.

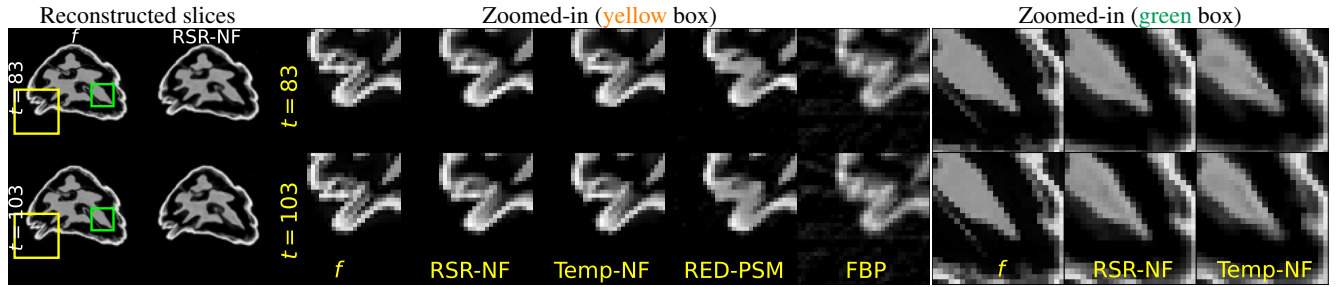


Figure 8. Comparison of reconstructed object frames for dynamic walnut at two time instants using different methods for $P = 128$, and the corresponding normalized absolute reconstruction errors.

[15] J. P. Haldar and Z.-P. Liang, “Spatiotemporal imaging with partially separable functions: A matrix recovery approach,” in *2010 IEEE Int. Symp. Biomed. Imaging*, April 2010, pp. 716–719.

[16] B. Zhao *et al.*, “Image reconstruction from highly undersampled (k , t)-space data with joint partial separability and sparsity constraints,” *IEEE Transactions on Medical Imaging*, vol. 31, no. 9, pp. 1809–1820, 2012. 1

[17] S. Babu, S. G. Lingala, and N. Vaswani, “Fast low rank column-wise compressive sensing for accelerated dynamic MRI,” *IEEE Transactions on Computational Imaging*, 2023. 1

[18] J. Yoo *et al.*, “Time-dependent deep image prior for dynamic MRI,” *IEEE Transactions on Medical Imaging*, vol. 40, no. 12, pp. 3337–

3348, 2021. 2, 5, 7

[19] Q. Zou *et al.*, “Dynamic imaging using a deep generative storm (GenStORM) model,” *IEEE Transactions on Medical Imaging*, vol. 40, no. 11, pp. 3102–3112, 2021. 2

[20] A. H. Ahmed *et al.*, “Dynamic imaging using deep bi-linear unsupervised representation (DEBLUR),” *IEEE Transactions on Medical Imaging*, vol. 41, no. 10, pp. 2693–2703, 2022. 1, 2

[21] L. Lozenski, M. A. Anastasio, and U. Villa, “A memory-efficient self-supervised dynamic image reconstruction method using neural fields,” *IEEE Transactions on Computational Imaging*, vol. 8, pp. 879–892, 2022. 1, 2, 3, 6

[22] L. Lozenski *et al.*, “ProxNF: Neural field proximal training for

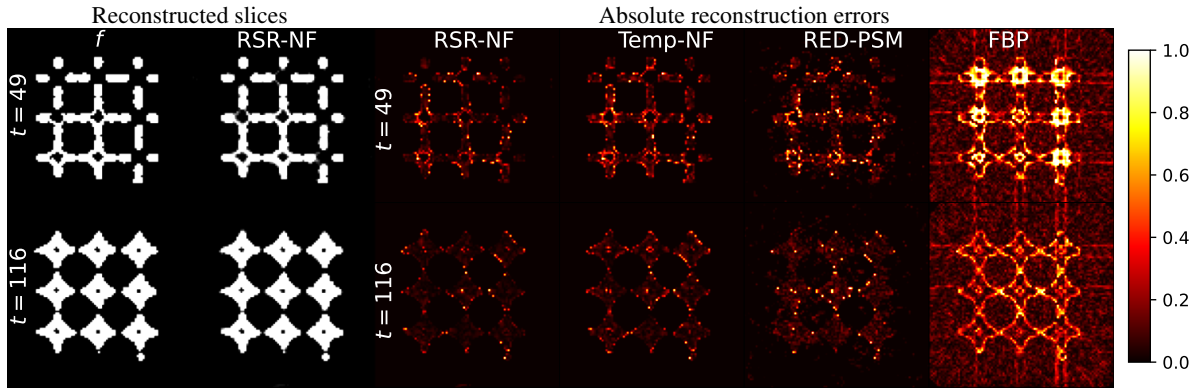


Figure 9. Comparison of ground-truth and RSR-NF reconstructed object frames at two time instants for $P = 128$, and the corresponding normalized absolute reconstruction errors using different methods for compressed polymer object subinterval.

- high-resolution 4D dynamic image reconstruction,” *arXiv preprint arXiv:2403.03860*, 2024. 1, 2
- [23] W. Xian *et al.*, “Space-time neural irradiance fields for free-viewpoint video,” in *Proceedings of the IEEE/CVF Conference on Computer Vision and Pattern Recognition*, 2021, pp. 9421–9431. 1
- [24] Z. Li *et al.*, “Neural scene flow fields for space-time view synthesis of dynamic scenes,” in *Proceedings of the IEEE/CVF Conference on Computer Vision and Pattern Recognition*, 2021, pp. 6498–6508.
- [25] Y. Du *et al.*, “Neural radiance flow for 4D view synthesis and video processing,” in *2021 IEEE/CVF International Conference on Computer Vision (ICCV)*. IEEE Computer Society, 2021, pp. 14 304–14 314.
- [26] K. Park *et al.*, “Nerfies: Deformable neural radiance fields,” in *Proceedings of the IEEE/CVF International Conference on Computer Vision*, 2021, pp. 5865–5874.
- [27] K. Park *et al.*, “HyperNeRF: A higher-dimensional representation for topologically varying neural radiance fields,” *ACM Trans. Graph.*, vol. 40, no. 6, dec 2021. 2
- [28] C. Gao *et al.*, “Dynamic view synthesis from dynamic monocular video,” in *Proceedings of the IEEE International Conference on Computer Vision*, 2021.
- [29] C. Wang *et al.*, “Neural trajectory fields for dynamic novel view synthesis,” *arXiv preprint arXiv:2105.05994*, 2021. 1
- [30] H. Pedersen *et al.*, “k-t PCA: temporally constrained k-t BLAST reconstruction using principal component analysis,” *Magnetic Resonance in Medicine: An Official Journal of the International Society for Magnetic Resonance in Medicine*, vol. 62, no. 3, pp. 706–716, 2009. 1
- [31] J. P. Haldar and Z.-P. Liang, “Low-rank approximations for dynamic imaging,” in *2011 IEEE International Symposium on Biomedical Imaging: From Nano to Macro*. IEEE, 2011, pp. 1052–1055.
- [32] B. Zhao *et al.*, “Further development of image reconstruction from highly undersampled (k, t)-space data with joint partial separability and sparsity constraints,” in *2011 IEEE International Symposium on Biomedical Imaging: From Nano to Macro*. IEEE, 2011, pp. 1593–1596.
- [33] S. G. Lingala and M. Jacob, “Blind compressive sensing dynamic MRI,” *IEEE transactions on medical imaging*, vol. 32, no. 6, pp. 1132–1145, 2013.
- [34] Y. Djebra *et al.*, “Manifold learning via linear tangent space alignment (LTSA) for accelerated dynamic MRI with sparse sampling,” *IEEE Transactions on Medical Imaging*, 2022. 1
- [35] S. G. Lingala *et al.*, “Accelerated dynamic MRI exploiting sparsity and low-rank structure: kt SLR,” *IEEE transactions on medical imaging*, vol. 30, no. 5, pp. 1042–1054, 2011. 1
- [36] A. Majumdar and R. Ward, “Learning space-time dictionaries for blind compressed sensing dynamic MRI reconstruction,” in *2015 IEEE International Conference on Image Processing (ICIP)*. IEEE, 2015, pp. 4550–4554.
- [37] J. D. Trzasko, “Exploiting local low-rank structure in higher-dimensional MRI applications,” in *Wavelets and Sparsity XV*, vol. 8858. SPIE, Sep. 2013, pp. 551–558. [Online]. Available: <https://www.spiedigitallibrary.org/conference-proceedings-of-spie/8858/885821/Exploiting-local-low-rank-structure-in-higher-dimensional-MRI-applications/10.1117/12.2027059.full> 1
- [38] M. Chiew *et al.*, “k-t FASTER: acceleration of functional MRI data acquisition using low rank constraints,” *Magnetic resonance in medicine*, vol. 74, no. 2, pp. 353–364, 2015. 1
- [39] R. Otazo, E. Candes, and D. K. Sodickson, “Low-rank plus sparse matrix decomposition for accelerated dynamic MRI with separation of background and dynamic components,” *Magnetic resonance in medicine*, vol. 73, no. 3, pp. 1125–1136, 2015. 1
- [40] S. G. Lingala, E. DiBella, and M. Jacob, “Deformation corrected compressed sensing (DC-CS): a novel framework for accelerated dynamic MRI,” *IEEE transactions on medical imaging*, vol. 34, no. 1, pp. 72–85, 2014. 2
- [41] X. Chen *et al.*, “Motion-compensated compressed sensing for dynamic contrast-enhanced mri using regional spatiotemporal sparsity and region tracking: Block low-rank sparsity with motion-guidance (blosm),” *Magnetic resonance in medicine*, vol. 72, no. 4, pp. 1028–1038, 2014.
- [42] H. Yoon, K. S. Kim, D. Kim, Y. Bresler, and J. C. Ye, “Motion adaptive patch-based low-rank approach for compressed sensing cardiac cine MRI,” vol. 33, no. 11, pp. 2069–2085, conference Name: IEEE Transactions on Medical Imaging. [Online]. Available: <https://ieeexplore.ieee.org/document/6832623>
- [43] A. Tolouee, J. Alirezaie, and P. Babyn, “Nonrigid motion compensation in compressed sensing reconstruction of cardiac cine MRI,” *Magnetic resonance imaging*, vol. 46, pp. 114–120, 2018. 2
- [44] D. Ulyanov, A. Vedaldi, and V. Lempitsky, “Deep image prior,” in *Proceedings of the IEEE conference on computer vision and pattern recognition*, 2018, pp. 9446–9454. 2
- [45] R. Hyder and M. S. Asif, “Generative models for low-rank video representation and reconstruction from compressive measurements,” in *2019 IEEE 29th International Workshop on Machine Learning for Signal Processing (MLSP)*. IEEE, 2019, pp. 1–6. 2
- [46] Y. Xie *et al.*, “Neural fields in visual computing and beyond,” in *Computer Graphics Forum*, vol. 41, no. 2. Wiley Online Library, 2022, pp. 641–676. 2
- [47] Y. Sun *et al.*, “Coil: Coordinate-based internal learning for tomographic imaging,” *IEEE Transactions on Computational Imaging*, vol. 7, pp. 1400–1412, 2021. 2, 3, 6

- [48] G. Zang *et al.*, “IntraTomo: self-supervised learning-based tomography via sinogram synthesis and prediction,” in *Proceedings of the IEEE/CVF International Conference on Computer Vision*, 2021, pp. 1960–1970.
- [49] L. Shen, J. Pauly, and L. Xing, “NeRP: implicit neural representation learning with prior embedding for sparsely sampled image reconstruction,” *IEEE Transactions on Neural Networks and Learning Systems*, 2022. 2
- [50] B. Song, L. Shen, and L. Xing, “Piner: Prior-informed implicit neural representation learning for test-time adaptation in sparse-view ct reconstruction,” in *Proceedings of the IEEE/CVF winter conference on applications of computer vision*, 2023, pp. 1928–1938. 2
- [51] A. W. Reed *et al.*, “Dynamic CT reconstruction from limited views with implicit neural representations and parametric motion fields,” in *Proceedings of the IEEE/CVF International Conference on Computer Vision*, 2021, pp. 2258–2268. 2
- [52] Y. Zhang *et al.*, “Dynamic cone-beam CT reconstruction using spatial and temporal implicit neural representation learning (STINR),” *Physics in Medicine & Biology*, vol. 68, no. 4, p. 045005, 2023. 2
- [53] L. Birklein *et al.*, “Neural deformable cone beam CT.” Eurographics, 2023. 2
- [54] J. Feng *et al.*, “Spatiotemporal implicit neural representation for unsupervised dynamic MRI reconstruction,” *arXiv preprint arXiv:2301.00127*, 2022. 2
- [55] W. Huang *et al.*, “Neural implicit k-space for binning-free non-cartesian cardiac MR imaging,” in *International Conference on Information Processing in Medical Imaging*. Springer, 2023, pp. 548–560.
- [56] V. Spieker *et al.*, “ICoNIK: Generating respiratory-resolved abdominal MR reconstructions using neural implicit representations in k-space,” in *International Conference on Medical Image Computing and Computer-Assisted Intervention*. Springer, 2023, pp. 183–192.
- [57] J. F. Kunz, S. Ruschke, and R. Heckel, “Implicit neural networks with fourier-feature inputs for free-breathing cardiac MRI reconstruction,” *arXiv preprint arXiv:2305.06822*, 2023. 2
- [58] E. D. Zhong *et al.*, “CryoDRGN: reconstruction of heterogeneous cryo-em structures using neural networks,” *Nature methods*, vol. 18, no. 2, pp. 176–185, 2021. 2
- [59] X. Wang *et al.*, “Neural radiance fields in medical imaging: Challenges and next steps,” *arXiv preprint arXiv:2402.17797*, 2024. 2
- [60] H.-C. Shao, T. Mengke, T. Pan, and Y. Zhang, “Dynamic CBCT imaging using prior model-free spatiotemporal implicit neural representation (PMF-STINR),” *ArXiv*, 2023. 2
- [61] K. Lee *et al.*, “Partition of unity networks: deep hp-approximation,” *arXiv preprint arXiv:2101.11256*, 2021. 2
- [62] R. Vo *et al.*, “Neural field regularization by denoising for 3D sparse-view x-ray computed tomography,” in *2024 International Conference on 3D Vision (3DV)*. IEEE, 2024, pp. 1166–1176. 2, 4
- [63] J. Liu, Y. Sun, C. Eldeniz, W. Gan, H. An, and U. S. Kamilov, “RARE: Image reconstruction using deep priors learned without groundtruth,” *IEEE Journal of Selected Topics in Signal Processing*, vol. 14, no. 6, pp. 1088–1099, 2020. 2, 4
- [64] Y. Romano *et al.*, “The little engine that could: Regularization by denoising (RED),” *SIAM J. Imaging Sci.*, vol. 10, no. 4, pp. 1804–1844, 2017. 2, 4, 5
- [65] R. Liu *et al.*, “Recovery of continuous 3D refractive index maps from discrete intensity-only measurements using neural fields,” *Nature Machine Intelligence*, vol. 4, no. 9, pp. 781–791, 2022. 3
- [66] N. Rahaman *et al.*, “On the spectral bias of neural networks,” in *International conference on machine learning*. PMLR, 2019, pp. 5301–5310. 3
- [67] S. V. Venkatakrishnan, C. A. Bouman, and B. Wohlberg, “Plug-and-play priors for model based reconstruction,” in *2013 IEEE global conference on signal and information processing*. IEEE, 2013, pp. 945–948. 4
- [68] U. S. Kamilov *et al.*, “Plug-and-play methods for integrating physical and learned models in computational imaging: Theory, algorithms, and applications,” *IEEE Signal Processing Magazine*, vol. 40, no. 1, pp. 85–97, 2023. 4
- [69] C. Metzler *et al.*, “prDeep: robust phase retrieval with a flexible deep network,” in *International Conference on Machine Learning*. PMLR, 2018, pp. 3501–3510. 4
- [70] Y. Sun *et al.*, “Block coordinate regularization by denoising,” *Advances in Neural Information Processing Systems*, vol. 32, 2019. 4
- [71] G. Mataev, P. Milanfar, and M. Elad, “DeepRED: Deep image prior powered by RED,” in *Proceedings of the IEEE/CVF International Conference on Computer Vision Workshops*, 2019, pp. 0–0. 4
- [72] E. T. Reehorst and P. Schniter, “Regularization by denoising: Clarifications and new interpretations,” *IEEE Transactions on Computational Imaging*, vol. 5, no. 1, pp. 52–67, 2018. 4
- [73] Y. Hu *et al.*, “A restoration network as an implicit prior,” *arXiv preprint arXiv:2310.01391*, 2023. 4
- [74] Y. Hu *et al.*, “Stochastic deep restoration priors for imaging inverse problems,” *arXiv preprint arXiv:2410.02057*, 2024. 4, 5
- [75] D. Gabay and B. Mercier, “A dual algorithm for the solution of nonlinear variational problems via finite element approximation,” *Computers & mathematics with applications*, vol. 2, no. 1, pp. 17–40, 1976. 4
- [76] J. Eckstein and D. P. Bertsekas, “On the Douglas—Rachford splitting method and the proximal point algorithm for maximal monotone operators,” *Mathematical Programming*, vol. 55, no. 1, pp. 293–318, 1992. 4
- [77] K. Zhang *et al.*, “Beyond a Gaussian denoiser: residual learning of deep CNN for image denoising,” *IEEE Transactions on Image Processing*, vol. 26, no. 7, pp. 3142–3155, 2017. 4
- [78] M. Delbracio and P. Milanfar, “Inversion by direct iteration: An alternative to denoising diffusion for image restoration,” *arXiv preprint arXiv:2303.11435*, 2023. 5
- [79] H. Der Sarkissian *et al.*, “A cone-beam X-ray computed tomography data collection designed for machine learning,” *Scientific data*, vol. 6, no. 1, p. 215, 2019. 5
- [80] “Piecewise Affine Transformation,” https://scikit-image.org/docs/dev/auto_examples/transform/plot_pieewise_affine.html. 5
- [81] D. P. Kingma and J. Ba, “Adam: A method for stochastic optimization,” *arXiv preprint arXiv:1412.6980*, 2014. 5
- [82] S. Kulkarni, J. A. Rumberger, and S. Jha, “Electron beam CT: A historical review,” *American Journal of Roentgenology*, vol. 216, no. 5, pp. 1222–1228, 2021, publisher: American Roentgen Ray Society. 6
- [83] D. Spronk *et al.*, “Evaluation of carbon nanotube x-ray source array for stationary head computed tomography,” *Med. Phys.*, vol. 48, no. 3, pp. 1089–1099, 2021. 6
- [84] S. Xu *et al.*, “Volumetric computed tomography with carbon nanotube x-ray source array for improved image quality and accuracy,” *Commun Eng*, vol. 2, no. 1, pp. 1–9, Oct. 2023, number: 1 Publisher: Nature Publishing Group. 6
- [85] G. Yüce *et al.*, “A structured dictionary perspective on implicit neural representations,” in *Proceedings of the IEEE/CVF Conference on Computer Vision and Pattern Recognition*, 2022, pp. 19 228–19 238. 6
- [86] Z. Wang *et al.*, “Image quality assessment: from error visibility to structural similarity,” *IEEE Transactions on Image Processing*, vol. 13, no. 4, pp. 600–612, 2004. 6
- [87] S. Ravishanker and Y. Bresler, “MR image reconstruction from highly undersampled k-space data by dictionary learning,” *IEEE Transactions on Medical Imaging*, vol. 30, no. 5, pp. 1028–1041, 2010. 6

Supplementary Material

5.1. Experimental configurations

The parameter selections for the experiments listed in Table 1 are provided in Table 2. Also, the architectural information for the DnCNN restoration networks used throughout this work is in Table 3. Finally, we provide parameter configurations for reconstructions in Figure 5 with different number of distinct view angles \hat{P} with $P = 128$ for both objects in Table 4.

		(a) Walnut			(b) Polymer		
P	Method	λ	ξ	β	λ	ξ	β
32	Temp-NF	-	1e+2	-	-	1e+2	-
32	RSR-NF	1e+0	1e+2	1e+0	1e+0	1e+2	1e+0
64	Temp-NF	-	1e+2	-	-	1e+1	-
64	RSR-NF	1e-1	1e+2	1e-1	1e+0	1e+1	1e+0
128	Temp-NF	-	1e+2	-	-	1e+2	-
128	RSR-NF	1e-1	1e+2	1e-1	1e+0	1e+2	1e+0

Table 2. The parameter selections for the reconstructions in Table 1.

Dataset	# of layers	# of channels
Walnut	6	64
Polymer	6	64

Table 3. Restoration network DnCNN configurations for different datasets.

		(a) Walnut			(b) Polymer		
\hat{P}	Method	λ	ξ	β	λ	ξ	β
4	Temp-NF	-	1e+2	-	-	1e+2	-
8	Temp-NF	-	1e+2	-	-	1e+2	-
16	Temp-NF	-	1e+2	-	-	1e+2	-
32	Temp-NF	-	1e+2	-	-	1e+2	-
4	RSR-NF	1e+0	1e+2	1e+0	1e+0	1e+2	1e+0
8	RSR-NF	1e+0	1e+2	1e+0	1e+0	1e+2	1e+0
16	RSR-NF	1e+0	1e+2	1e+0	1e+0	1e+2	1e+0
32	RSR-NF	1e+0	1e+2	1e+0	1e+0	1e+2	1e+0

Table 4. The parameter selections for the reconstructions with different number of distinct view angles \hat{P} in Figure 5 for $P = 128$.